Science
AAAS

Supplementary Materials for

Structural basis for allosteric PARP-1 retention on DNA breaks

Levani Zandarashvili, Marie-France Langelier, Uday Kiran Velagapudi,
Mark A. Hancock, Jamin D. Steffen, Ramya Billur, Zain M. Hannan,
Andrew J. Wicks, Dragomir B. Krastev, Stephen J. Pettitt,
Christopher J. Lord, Tanaji T. Talele, John M. Pascal, and Ben E. Black
Correspondence to: john.pascal@umontreal.ca, blackbe@pennmedicine.upenn.edu

This PDF file includes:

Extended Discussion

Our HXMS experiments allowed us to directly monitor changes in PARP-1 dynamics in the presence of inhibitors, when PARP-1 is bound to a DNA strand break. These results, along with our biochemical data, indicate that none of the clinical PARP-1 inhibitors exert a strong reverse allosteric effect on PARP-1 bound to DNA. In contrast some inhibitors, which we have designated Type III or allosteric pro-release inhibitors, have, in fact, an opposite effect to what was predicted: promoting a more folded conformation of the HD and decreasing PARP-1 affinity for DNA. Type II or non-allosteric inhibitors, which include the best trapping inhibitor talazoparib, have no substantial effect on PARP-1 allostery, although talazoparib and olaparib both exhibited some hints of biochemical characteristics that are consistent with pro-retention behavior. However, two non-clinical inhibitors (BAD and EB-47), which we have designated as Type I or allosteric pro-retention inhibitors, do show clear evidence of a strong reverse allosteric effect that increases PARP-1 retention on a DNA break. Through mutagenesis that breaks interdomain communication in PARP-1, or that disrupts contacts between the inhibitor and the HD, we show that we can abrogate the reverse allosteric effect of a Type I inhibitor and transform it into a Type II inhibitor.

With this level of understanding of PARP-1 allostery, we were able to directly test whether reverse allostery plays a role in the ability of an inhibitor to trap PARP-1 on chromatin by converting the Type III inhibitor veliparib into a Type I inhibitor, UKTT15. Veliparib and UKTT15 are similar in their abilities to inhibit PAR formation in the cell. However, UKTT15 shows a clear reverse allosteric effect on the PARP-1 HD and regulatory domains and increases retention of PARP-1 on DNA breaks biochemically. Our chromatin fractionation and laser irradiation assays in cells indicate that UKTT15 is more efficient than veliparib at retaining PARP-1 on DNA, and that this potential correlates with enhanced killing of cancer cells that carry deleterious mutations in the *BRCA* genes (CAPAN-1 and SUM149PT). However, we also found that UKTT15 is more efficient than veliparib at killing SUM149PT-BRCA1$_{rev}$ cells that have restored BRCA1 function and thus has a shifted therapeutic window (but of similar magnitude) relative to veliparib. UKTT15 thus serves as a proof-of-principle compound that allosteric SSB DNA retention can be engineered. It is possible that UKTT15 could be improved in its potency and drug-like properties (i.e. solubility and chemical stability [indeed, it is less soluble than veliparib and would seem a target for enzymatic hydrolysis of methyl ester group]). Future work to develop this compound through exploration of a diversity of functional groups, as well as exploration of other PARPi compound derivatives, that generate allosteric trapping has the promise to produce forms of PARPi that have 1) outstanding drug-like properties, 2) high potency of catalytic inhibition (e.g. those observed with talazoparib), and 3) allosteric pro-SSB DNA retention (e.g. what we observe with UKTT15).

In light of our work, it is interesting to consider how the current set of PARPi exert their cellular trapping properties. An important first example is talazoparib, which does not exert a pronounced reverse allosteric effect on PARP-1, yet is very efficient at trapping PARP-1 on chromatin. In this case, the difference in inhibitory potency that we show in cells, combined with a slow dissociation half-life (*19*) and a largely neutral effect on the HD might explain its high trapping effect. In contrast, other inhibitors in the Type III allosteric pro-release class apply opposite forces on the HD that would contribute to

lowering their ability to trap PARP-1 in the cell efficiently. However, this effect could be compensated partly in the case of some of these inhibitors by a higher inhibitory potency and/or slower dissociation half-life still allowing them to trap PARP-1 on DNA breaks and kill cancer cells (Fig. 6). For instance, Type III inhibitor, niraparib, achieves reasonable cellular trapping behavior (*21*), apparently by strong catalytic inhibition that limits automodification-dependent SSB DNA release as well as long half-lives/slow clearance rates (*21*, *26*, *30*, *31*). Veliparib is universally considered a poor trapper, and we note that it has several characteristics favoring release from breaks: the Type III pro-release allosteric behavior, relatively low catalytic inhibition potency and high dissociation rate from PARP-1 (*24*), and relatively rapid clearance rates *in vivo* (*25*, *40*).

Consistent with our model, a recent study shows that rucaparib and talazoparib, despite exhibiting similar inhibitory potency in cells and binding properties to PARP-1, show much more pronounced differences in trapping abilities (*41*). We attribute these differences to the propensity of rucaparib to promote stabilization of the HD, which in turn decreases PARP-1 affinity for DNA and its retention time on DNA breaks. The catalytic inhibition differences between PARPi are critical to consider, here. For example, a recent single-molecule tracking experiment with quantum-dot labeled PARP-1 on DNA tightropes indicated that even a low level of PARP-1 automodification led to constrained motion at a DNA break site (*42*). Thus, it could be that even subtle differences in PARPi potencies could give rise to differences in automodification levels that yield significant differences in PARP-1 mobility, or interaction potential with other repair factors, and thus trapping potential.

Finally, we consider the idea that the allosteric communication pathway is relevant for PARPi resistance mechanisms that arise in patients. The R591C PARP-1 mutation was recently identified in the diagnostic biopsy of a *de novo* PARPi resistant patient with ovarian cancer (*33*). In cell localization experiments, the R591C mutant was recruited to sites of microirradiation, but dissociated quickly from damage sites and was not trapped by talazoparib. Based on our results, we propose that the R591C mutant with its disrupted interdomain communication and reduced DNA binding ability is unable to be trapped on DNA by PARPi, regardless of their abilities to induce reverse allostery in the WT protein. The abnormal DNA binding behavior of the R591C mutant likely participates in its resistance to PARPi, since this mutant might never be able to bind strongly enough to DNA to become a toxic lesion for the cell. We predict that other categories of resistance mutations could be found after exposure to reverse allosteric inhibitors such as UKTT15 in the region where UKTT15 contacts the HD at the N-terminal end of the αF helix.

Materials and Methods

Protein expression and purification

Full-length PARP-1 WT and mutants' expression and purification were described previously (*4*). PARP-1 CAT WT (residues 661 to 1014), CAT WT (residues 661 to 1011; used in crystallization), and CATΔHD were expressed and purified as described (*5*). Note that for CATΔHD and PARP-1 overactive mutant D766/D770A, 10 mM benzamide was added to the *E.coli* media to reduce cellular toxicity due to PARP-1 activity.

HXMS measurement and analysis

Prior to deuterium on-exchange reaction, PARP-1 and SSB-DNA were mixed at final concentrations of 2.6 μM and 5 μM, respectively, in 10 mM HEPES, pH 7.0, 150 mM NaCl, 0.1 mM TCEP, and incubated at least 30 min at room temperature afterwards, to allow the complex formation. An inhibitor was added at a final concentration of 5.2 μM and incubated at room temperature for at least 15 min, where applicable. Deuterium on-exchange was carried out at RT by mixing 5 μL of each sample with 15 μL of deuterium on-exchange buffer (10 mM HEPES, pD 7.0, 150 mM NaCl, in D_2O) yielding a final D_2O concentration of 75%. pD values for deuterium-based buffers were calculated as pD = pH + 0.4138. Upon mixing with on-exchange buffer, the amide protons will be replaced over time with deuterons yielding an increased peptide mass. To quench the deuterium exchange reaction, the sample (20 μl) was mixed with 30 μl of ice-cold quench buffer (1.66 M guanidine hydrochloride, 10% glycerol, and 0.8% formic acid, for a final pH of 2.4–2.5) and rapidly frozen in liquid nitrogen, stored at -80 C until further use. For the MS analysis, each sample (50 μL) was melted on ice and loaded onto an in-house packed pepsin column for digestion. Pepsin (Sigma) was coupled to POROS 20 AL support (Applied Biosystems), and the immobilized pepsin was packed into a column housing (2 mm × 2 cm, Upchurch). Pepsin-digested peptides were captured on TARGA C8 5 μm Piccolo HPLC column (1.0 × 5.0 mm, Higgins Analytical) and eluted through an analytical C18 HPLC column (0.3 × 75 mm, Agilent) by a shaped 12–100% buffer B gradient at 6 μL/min (Buffer A: 0.1% formic acid; Buffer B: 0.1% formic acid, 99.9% acetonitrile). The effluent was electrosprayed into the mass spectrometer. Non-deuterated (ND) PARP-1 samples were prepared in 10 mM HEPES, pH 7.0, 150 mM NaCl buffer, and mixed with the quench buffer to mimic the samples from on-exchange reaction. Peptides of ND samples were analyzed in tandem MS (LTQ Orbitrap XL, Thermo Fisher Scientific). We analyzed MS/MS data collected from these samples to identify potential PARP-1 peptides using SEQUEST (Bioworks v3.3.1, Thermo Fisher Scientific) with a peptide tolerance of 8 ppm and a fragment tolerance of 0.1 AMU. Deuterated samples were then analyzed on an Exactive Plus EMR-Orbritrap (Thermo Fisher Scientific). A MATLAB based program, ExMS was used to prepare the pool of peptides based on SEQUEST output files. HDExaminer software was next used to process and analyze the HXMS data. HDExaminer identifies the peptide envelope centroid values for non-deuterated as well as deuterated peptides and uses the information to calculate the level of peptide deuteration for each peptide at each timepoint. Each individual deuterated peptide is corrected for loss of deuterium label during HXMS data collection (i.e., back exchange after quench) by normalizing to the maximal deuteration level of that peptide, which we measure in a “fully deuterated” (FD) reference sample. The FD sample was prepared in 75% deuterium to mimic the exchange experiment, but under acidic denaturing conditions (0.5% formic acid), and incubated over 48 h to allow each amide proton position along the entire polypeptide to undergo full exchange. HDExaminer performs such correction automatically when provided with the FD file. For each peptide, we compare the extent of deuteration as measured in the FD sample to the theoretical maximal deuteration (i.e., if no back-exchange occurs); the median extent of back-exchange in our datasets is only 15%.

HXMS plotting

Peptide plotting was performed in MATLAB using deuteration levels for each peptide extracted from the HDExaminer outputs. Differences in deuteration levels between two samples were calculated for all peptides for which the identical peptide was found in both conditions (e.g., PARP-1/DNA complex with and without EB-47), the ND, and FD samples. For comparing two different HXMS datasets, we plot the percent difference of each peptide, which is calculated by subtracting the percent deuteration of one sample from that of another, and plotted according to the color legend in stepwise increments (as in Fig. S1). We include in our figures peptides of identical sequence but different charge states. Although not unique peptides, they do add confidence to our peptide identification as their deuteration levels are in close agreement with each other. Consensus behavior at each residue was calculated as the average of the differences in HX protection of all peptides spanning that residue (as in Fig. 1B and S1). For the plot of peptide data expressed as the number of deuterons (e.g. Fig. 3B, 4C and S3), the values are expressed as the mean of three independent measurements + /− s.d.

Differential scanning fluorimetry (DSF)

DSF experiments were performed mainly as described (*5*, *6*, *43*) using 5 μM of protein and 1 mM inhibitor on a Roche LightCycler 480 RT-PCR. ΔT_M values were calculated by subtracting the T_M determined for the protein in the absence of compound from the T_M determined in the presence of compound. Experiments were performed in triplicate and a Boltzmann sigmoid was fit to the data to determine the T_M values (KaleidaGraph).

Fluorescence polarization

For the DNA competition assay, 40 nM PARP-1 WT was incubated with 20 nM dumbbell DNA with a central nick carrying an internal fluorescent FAM group (5' GCT GAG C/FAMT/T CTG GTG AAG CTC AGC TCG CGG CAG CTG GTG CTG CCG CGA) for 30 minutes at RT in 12 mM Hepes pH 8.0, 60 mM KCl, 8 mM $MgCl_2$, 4% glycerol, 5.7 mM beta-mercaptoethanol, 0.05 mg/ml BSA in the presence of inhibitors (100 μM). A competitor unlabelled DNA of the same sequence was added at 100 nM and FP was measured over time on a VictorV plate reader (Perkin Elmer). For DNA binding affinity measurements, increasing concentrations of PARP-1 were incubated for 30 min at RT with 5 nM of dumbbell DNA probe carrying a nick (described above) in the absence or presence of inhibitors (100 μM) in the following buffer: 12 mM Hepes pH 8.0, 250 mM NaCl, 4% glycerol, 5.7 mM beta-mercaptoethanol, 0.05 mg/ml BSA.

Surface plasmon resonance (SPR)

Binding between biotinylated DNA (24 kDa) and purified PARP-1 (113 kDa) was examined using a BIACORE 3000 system (GE Healthcare Bio-Sciences AB, Upsala, Sweden; BIAcontrol v4.1 software). Protein-grade detergents (Triton X-100 #APX100 and Empigen #D350) were purchased from Anatrace (Maumee, OH, USA) and neutravidin (Pierce #31000) was from Thermo Scientific (Waltham, MA, USA).

SPR surfaces were prepared on research-grade CM5 sensor chips (Biacore) at 25°C using filtered (0.2 μm) and degassed HBS-X150 buffer (10 mM Hepes, pH 7.4; 150 mM NaCl; 3 mM EDTA; 0.05% (v/v) Triton X-100). Neutravidin (2 mg/mL stock in

water) was immobilized to reference and active flow cells according to Biacore's recommendations (Amine Coupling Kit using 50 ug/mL neutravidin in 10 mM sodium acetate pH 5.0; approximately 10,000 RU per flow cell) and washed with 1 M sodium chloride (50 uL/min x 30 sec pulses). For active flow cells, biotinylated DNA dumbbell (SSB-DNA), or a single-stranded DNA as a control for DNA structure-specific binding, was captured on neutravidin-coated surfaces at 50 nM in HBS-X150 buffer and at 10 µL/min (approximately 300 RU per flow cell) and then washed with 0.5 M sodium chloride.

To assess binding specificity, kinetics, and affinity, PARP-1 (0 – 50 nM; 2-fold dilution series) was titrated over reference (neutravidin only), single-stranded DNA (negative control), and SSB-DNA surfaces in HBS-X250 buffer (same as HBS-X150, but containing 250 mM NaCl to prevent non-specific DNA binding) using single-cycle kinetics (70 µL/min x 3 m association + 1 – 10 min dissociation). Between the titration series, the immobilized DNA surfaces were regenerated at 50 µL/min using 30 s pulses of solutions I (HBS-X150 containing 1.0 M NaCl and 0.05% (v/v) Empigen), II (20 mM HCl), III (50 mM NaOH), IV (0.5% (w/v) SDS), and V (50 mM glycine pH 9.5). To examine the effect of PARPi on PARP-1 interaction with a DNA break, a fixed concentration of PARP-1 (30 nM) was injected in the absence (HBS-X250 buffer containing 5% (v/v) DMSO) or presence of inhibitors (50 µM during both the association and dissociation phases) using the 'COINJECT' command (50 µL/min for 2 m association + 5 m dissociation) followed by an approximately 8 min "wash out" period (DMSO-containing buffer without inhibitor).

All SPR data were doubled-referenced (*44*) and are representative of duplicate injections acquired from at least three independent trials. For each COINJECT series, 30 nM PARP-1 only injections before and after the inhibitor-containing injections ensured that there was no significant loss in surface activity throughout each assay. Experimental signal responses were also verified against the theoretical binding maxima predicted by the following equation: Rmax = MWA / MWL * RL * n where Rmax is the maximal binding response (RU) at saturating PARP-1 concentration; MWA is the molecular mass (kDa) of PARP-1; MWL is the molecular mass (kDa) of the immobilized DNA; RL is the amount (RU) of immobilized DNA; and n is the predicted binding stoichiometry (1:1). In the absence of PARP-1 inhibitors, apparent equilibrium dissociation constants ($K_D = k_d / k_a$; nM) were determined by global fitting of the single-cycle data to a ''1:1 titration" model (*45*) in the BIAevaluation v4.1 software. In the presence of PARP-1 inhibitors, dissociation rate constants (k_d; s^{-1}) were determined at the beginning of the dissociation phase (averaged at 430 – 440 s to avoid any potential rebinding effects later in the dissociation phase) using the BIAevaluation "Fit Kinetics, Separate k_a/k_d" tool.

Chromatin fractionation

CAPAN-1 cells were plated at a concentration of 190 cells/µL in a total volume of 4 mL DMEM/10% FBS media in 6 well plates and grown for 48 h. Inhibitors (500 µL) at various concentrations were added and the cells were incubated for 30 min at 37°C. MMS was added (500 µL) at a final concentration of 0.01% and incubated for 3 h at 37°C. Cells were washed with PBS, treated with 350 µL trypsin-EDTA, collected and fractionated using the Subcellular Fractionation Kit (Thermo Fisher) following the

manufacturer's protocol. Chromatin fractions were analyzed by Western Blot using the anti-PARP-1 C2-10 antibody (1:5000) and anti-H3 3H1 antibody (1:750) as a loading control along with a Ponceau-S staining of the membrane.

Measurement of PAR in cells

CAPAN-1 cells (80 μL) were plated at a concentration of 67 cells/μL in a 96 well plate and grown for 4 days. 10 μL of various concentrations of inhibitors diluted in DMEM/10% FBS containing 10% DMSO were added to the wells and incubated for 30 min. at 37°C. 10 μL of MMS 0.1% in DMEM/10% FBS were added to the wells and incubated for 1 hour at 37°C. Cells were washed with PBS and lysed by the addition of 50 μL of CelLytic M buffer (Sigma) to which the PARG inhibitor ADP-HPD was added (0.1 mM final) following the manufacturer's protocol. Whole cell extracts were analyzed by Western Blot using the anti-pan-ADP-ribose binding reagent (1:1500, MABE1016, Millipore Sigma) and the membrane was stained using Ponceau-S for a loading control.

Cell survival assay

90 μL of CAPAN-1 cells were plated at 17 cells/μL in a 96 well plate in DMEM/10% FBS. 10 μL of inhibitors at various concentrations in DMEM/10% FBS/10% DMSO were added (final concentration of DMSO of 1% in well). Cells were incubated for 7 days at 37 °C, 5 % CO_2. The media was exchanged on day 4 with 100 μL fresh media DMEM/10% FBS/10% DMSO containing inhibitors. The number of live cells was measured using either the Cell Titer Glo 2.0 assay (Promega) or the ATPlite luminescence assay (PerkinElmer) following the manufacturer's protocol. The SUM149PT cells were grown in Ham's media with 5% FBS supplemented with hydrocortisone (1 μg/mL), insulin (5 μg/mL) and Hepes (10 mM pH 8.0) according to the manufacturer's recommendation. For the assay, 10 μL of SUM149PT cells were plated at 170 cells/μL in a 96 well plate in the SUM149PT complete media described above supplemented with 1% DMSO. 90 μL of inhibitors at various concentrations diluted in complete media/1% DMSO were added. The drug dilutions were spun prior to plating in order to avoid transferring any precipitate that could have formed. Cells were incubated for 7 days at 37 °C, 5 % CO_2. The media was exchanged on day 4 with 100 μL fresh complete media/1% DMSO containing inhibitors. The number of live cells was measured as described above. SUM149PT cells were acquired from Roger A. Greenberg (Penn).

Microirradiation assays

For microirradiation, CAL51 PARP-1$^{-/-}$ cells, stably complemented with PARP-1-GFP expressing cDNA, were seeded in glass-bottom culture dishes (MaTek, P35G-0.170-14-C) and incubated for 24 h. Drugs were added 1 h prior imaging. Imaging was conducted on Andor Advance Spinning Disk microscope, 100x oil immersion objective with micropoint at 365 nm and irradiated circular area with 1 μm diameter. The background intensity of an area in the nucleus was subtracted from the irradiated area intensity and the maximum was normalized to one. For each experiment more than 50 cells were imaged in biological replicates (*46*).

Protein crystallization and structure determination

PARP-1 CATΔHD (30 mg/ml) was crystallized in the presence of 1.1 mM UKTT15 in 18 to 20% PEG 3350, 0.2 M Ammonium Sulfate, 0.1 M Sodium Citrate pH 5.6 in sitting drop vapor diffusion trays at room temperature. Crystals were cryo-protected (18% PEG 3350, 0.2 M Ammonium Sulfate, 0.1 M Sodium Citrate 5.6, 1.1 mM UKTT15, 20% sucrose) prior to flash-cooling in liquid nitrogen. X-ray diffraction data were collected at the Advanced Light Source (ALS) beamline 8.3.1 (Lawrence Berkeley Laboratory, California) and processed using XDS (*47*) (Supplementary Table S2). The structure was determined by molecular replacement using PHASER (*48*) as implemented in the Phenix suite (*49*) and PDB code 5ds3 (*4*) as a search model. PARP-1 CAT WT (residues 661 to 1011) was crystallized in complex with Rucaparib (0.5 mM), EB-47 (0.5 mM), and UKTT-15 (1.1 mM) by sitting drop vapor diffusion under the following conditions: 1.8 to 2.0 M Ammonium Sulfate, 100 mM Tris pH 8 (Rucaparib/EB-47) or Bis-Tris pH6.5 (UKTT-15), and 5% PEG 400 (Rucaparib/EB-47). The crystallization conditions were supplemented with 20% glycerol (Rucaparib/EB-47) or 20% sucrose (UKTT-15) as cryo-protectant for flash-cooling crystals in liquid nitrogen. CAT/Rucaparib and CAT/EB-47 crystal diffraction data was collected at ALS beamline 12.3.1; CAT/UKTT-15 crystal diffraction data was collected at ALS beamline 8.3.1. CAT/Rucaparib diffraction data was processed using XDS (*47*) (Supplementary Table S2), and the structure was determined by molecular replacement in PHENIX using PDB code 3gjw as a search model. CAT/UKTT-15 and CAT/EB-47 diffraction data were processed using MOSFLM and SCALA in the CCP4 suite (*50*). Patterson analysis of the CAT/UKTT-15 and CAT/EB-47 diffraction data (in PHENIX and SCALA) strongly indicated translational pseudo-symmetry/translational NCS, which commonly contributes to high crystallographic R factors during refinement (see Supplementary Table S2). Indeed, the diffraction patterns of CAT/UKTT-15 and CAT/EB-47 exhibited layers of weak and strong reflections that complicated data processing and refinement (e.g. R factors and phi/psi outliers; Table S2), but nevertheless resulted in structures that clearly indicated the binding poses of the inhibitors. CAT/UKTT-15 and CAT/EB-47 structures were determined by molecular replacement in PHENIX using the ART fold from PDB code 5ds3. The entire HD domain was then positioned manually into the resulting F_O-F_C difference maps that indicated the locations of several HD helices. The quality of the electron density in the HD region was of a much lower quality than that observed in the ART region (see Figures 4H and S6). We interpret the weaker electron density to indicate that the HD is poorly ordered/highly mobile in the context of bound UKTT-15 or EB-47. Correspondingly, the electron density for the bound inhibitors is better defined in the portion interacting with the ART, than the portion interacting with the HD. The density is quite weak in certain regions of the HD, but rather than delete these sections, we have opted to keep the entire HD in our final deposited model. All model building was performed using COOT (*51*), and refinement was performed using Phenix (*51*) and REFMAC5 (*50*, *52*). Structure images were made using PYMOL Molecular Graphics System (Schrödinger, LLC).

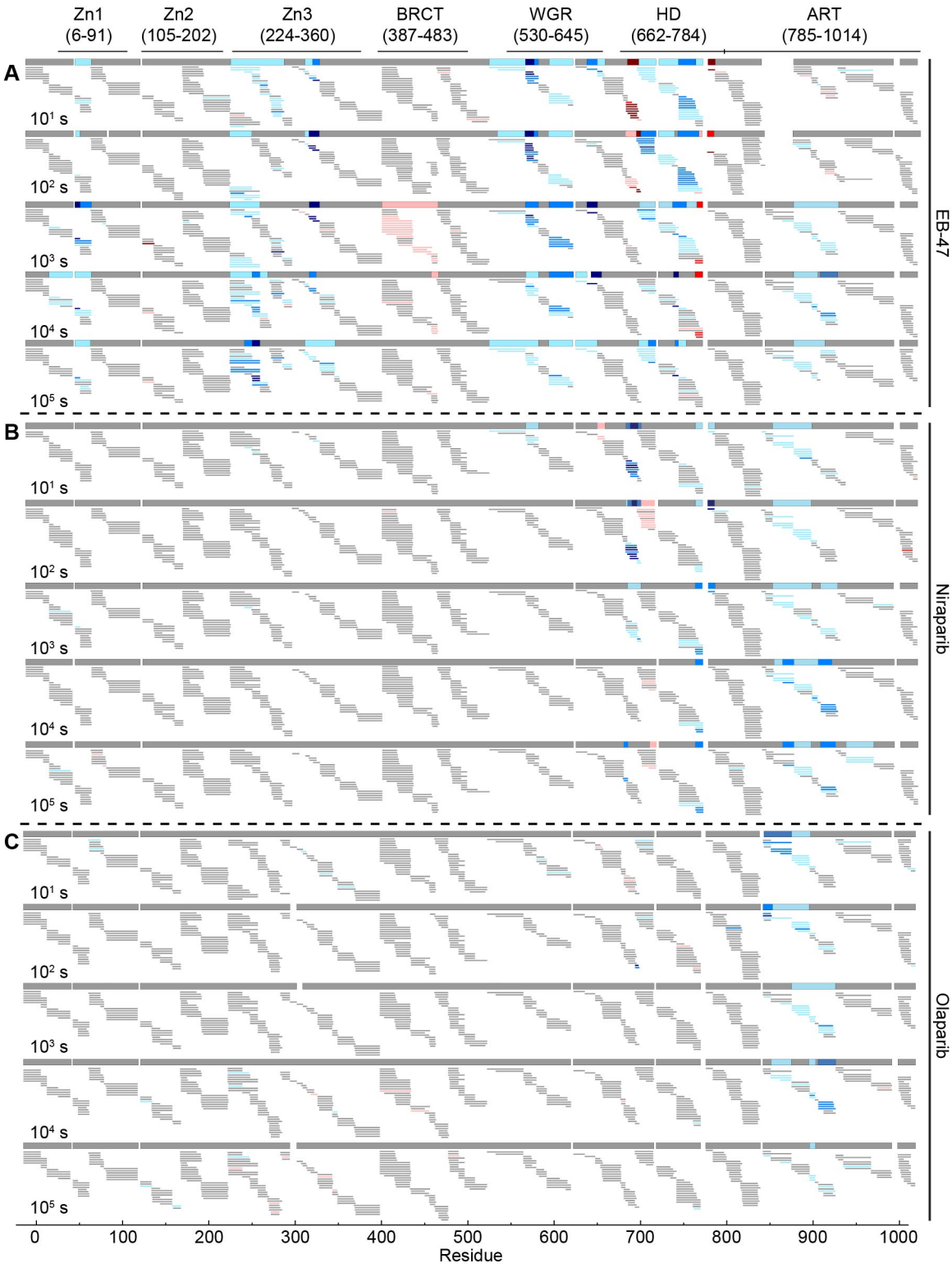
Zn1 (6-91)
Zn2 (105-202)
Zn3 (224-360)
BRCT (387-483)
WGR (530-645)
HD (662-784)
ART (785-1014)
A
B
C
10^1 s
10^2 s
10^3 s
10^4 s
10^5 s
EB-47
Niraparib
Olaparib
0
100
200
300
400
500
600
700
800
900
1000
Residue

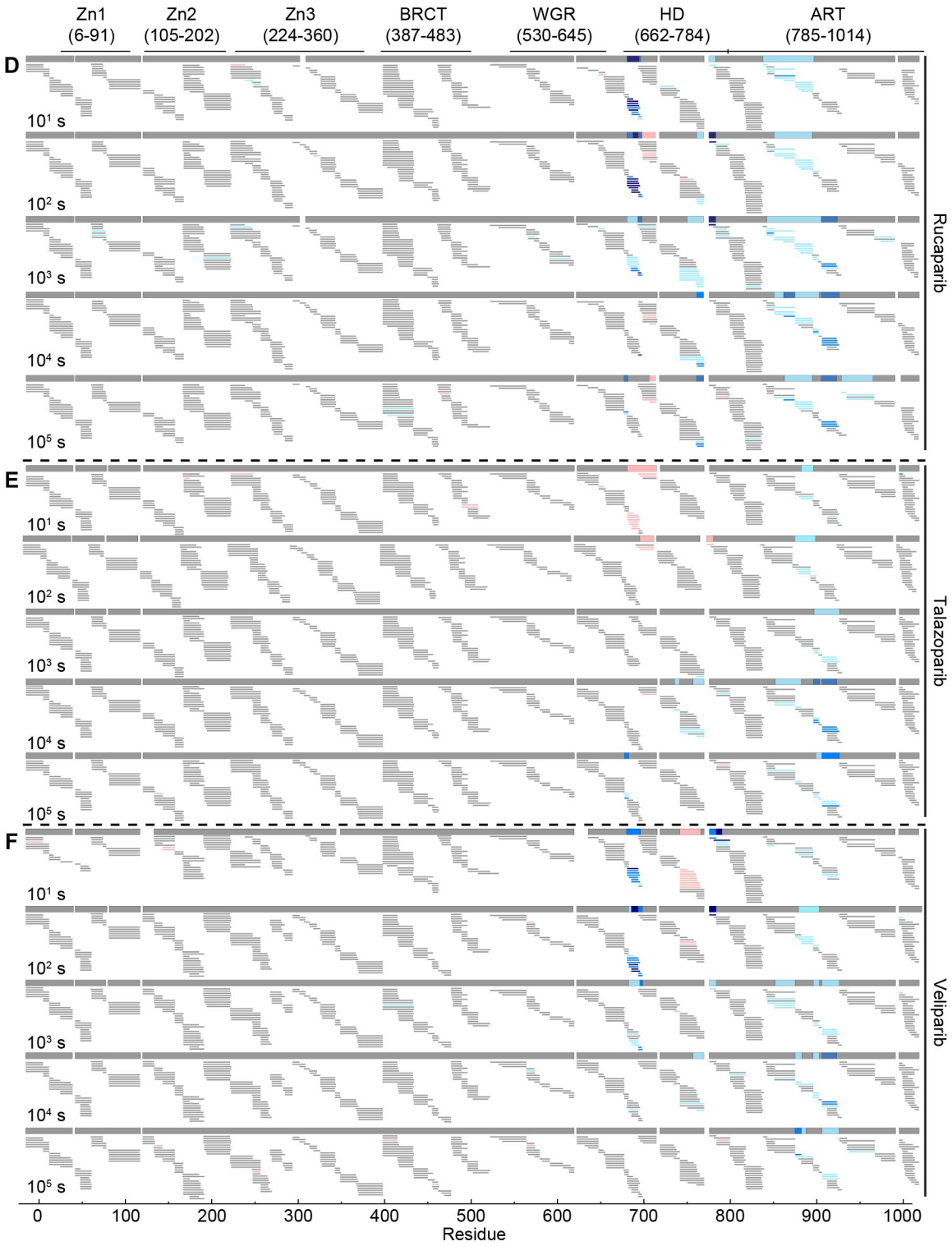

Figure S1: Difference plots for HX rates for each inhibitor relative to the sample without any inhibitors. (A-F) Peptide data corresponding to consensus plots in Fig. 1B. Percent difference in deuteration for each peptide (i.e. HX), represented with horizontal bars, was calculated between DNA-bound PARP-1 samples in the absence and presence of the indicated PARPi at five time points (10^1 – 10^5 s). These time points

were chosen based on our previous PARP-1 experiments (*4, 6*). The vast majority of all PARP-1 peptides experience essentially complete HX before the final time point. Peptides that exhibit increased protection from deuteration upon inhibitor binding are shown in blue colors (i.e. slower HX), whereas the ones with decreased protection from deuteration upon inhibitor binding are in red (i.e. faster HX). Each peptide color indicates the average percent difference in deuteration for the whole peptide; thus, there are some overlapping peptides where one exhibits a difference in deuteration pattern, whereas the other one does not. The consensus behavior at each PARP-1 residue is displayed in the horizontal bar for each time point. Gaps in protein coverage are indicated with white spaces. When available, data for multiple peptide charge states are presented. We observed the Type III (veliparib, rucaparib, and niraparib) PARPi-induced changes to the HD domain, but no measurable changes are observed in the DNA-contacting Zn1, Zn2, and Zn3 domains. This observation can be explained by the experimental conditions. Namely, to simplify the analysis of HXMS experiments, we perform them at PARP-1 concentrations (2.6 μM) that are substantially higher than the K_D for DNA in order to saturate binding of PARP-1 to SSB-DNA in all cases. Thus, the protection gained by binding to SSB DNA (*4*) is maintained, and only additional rigidity (i.e. what is observed with allosteric behavior of Type I PARPi [EB-47]) can be measured by HXMS. While no clinical PARPi that we studied exhibited strong Type I properties, it is notable that the Type II inhibitors (olaparib and talazoparib) are both considered strong cellular “trappers” (*21*, *27*, *31*) while at least one of the Type III inhibitors (veliparib) is thought to lack the ability to trap PARP-1 on DNA in the cell (*21*, *31*, *36*).

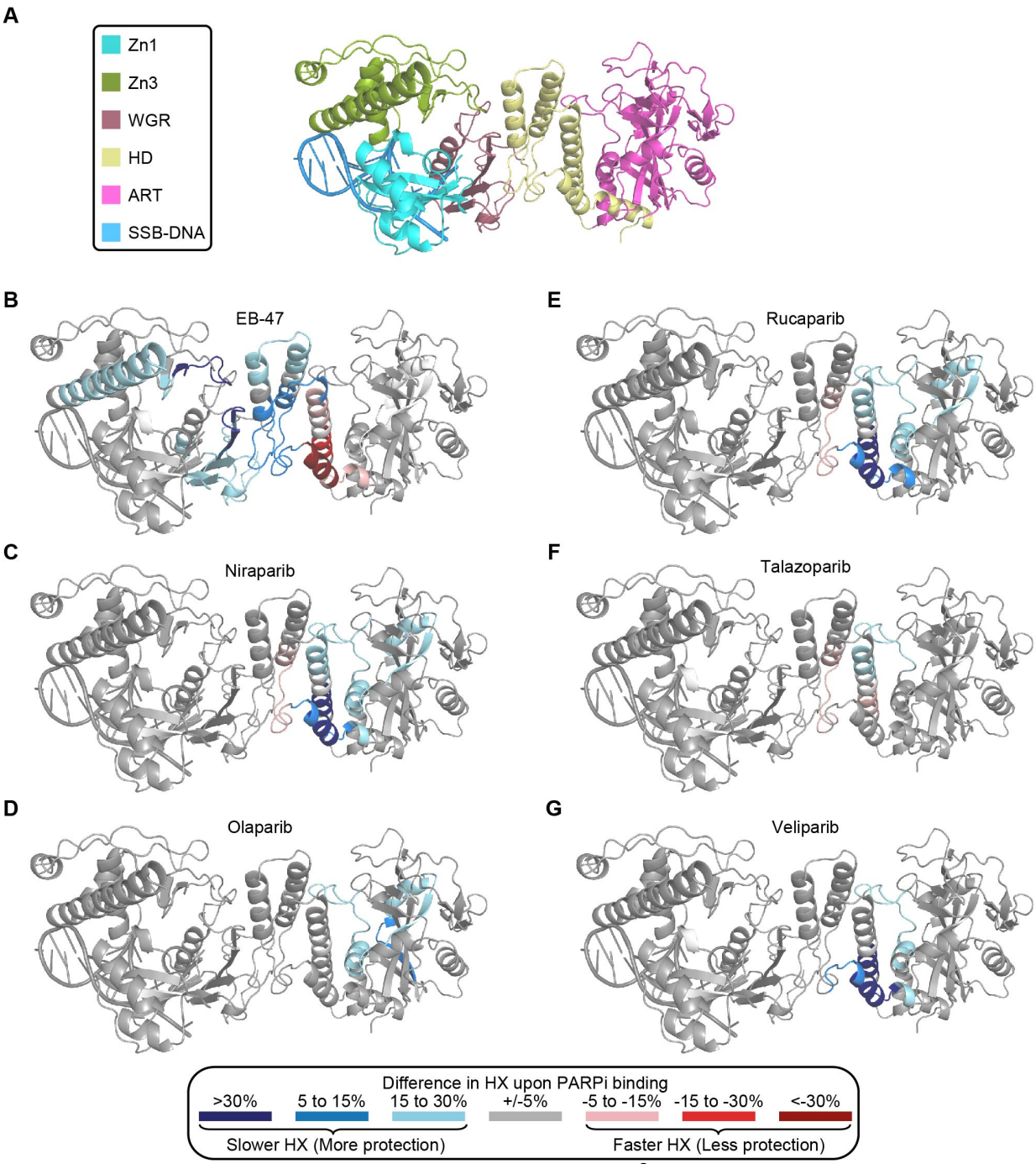

Figure S2: Consensus difference HXMS data at 10^2 s shown in Fig. 1B mapped on PARP-1 structure. (A) PARP-1/DNA complex structure as shown in Fig. 1C. (B-G) Percent changes in HX rates upon binding of the following inhibitors to PARP-1/DNA complex: (B) EB-47, (C) niraparib, (D) olaparib, (E) rucaparib, (F) talazoparib and (G) veliparib. The Type I PARPi, EB-47, causes greater destabilization of two HD helices (αB and αF), but there is protection in the adjacent HD regions that contact the WGR domain (αD and αE). There is subsequent protection at interdomain interfaces, connecting back to the DNA binding domains. Specifically, the key connections between the CAT domain back to the DNA binding domains are mediated by contacts between

the HD and the WGR and Zn3 domains (*5*, *39*, *53*, *54*). WGR forms a fairly broad interface with the HD. Zn3 forms a smaller direct interface with the HD. Zn1 is also indirectly connected to the HD through a different surface of WGR. These serve as the contact points that first come together upon activation by binding to a DNA break (*4*) and are subsequently the important sites for the 'reverse allostery' that exists upon binding to NAD^+. The HX behavior of the Type I PARPi, EB-47, led us to the strong prediction that this allosteric network is important for communication from the EB-47 binding site in the CAT domain back to the DNA binding domains.

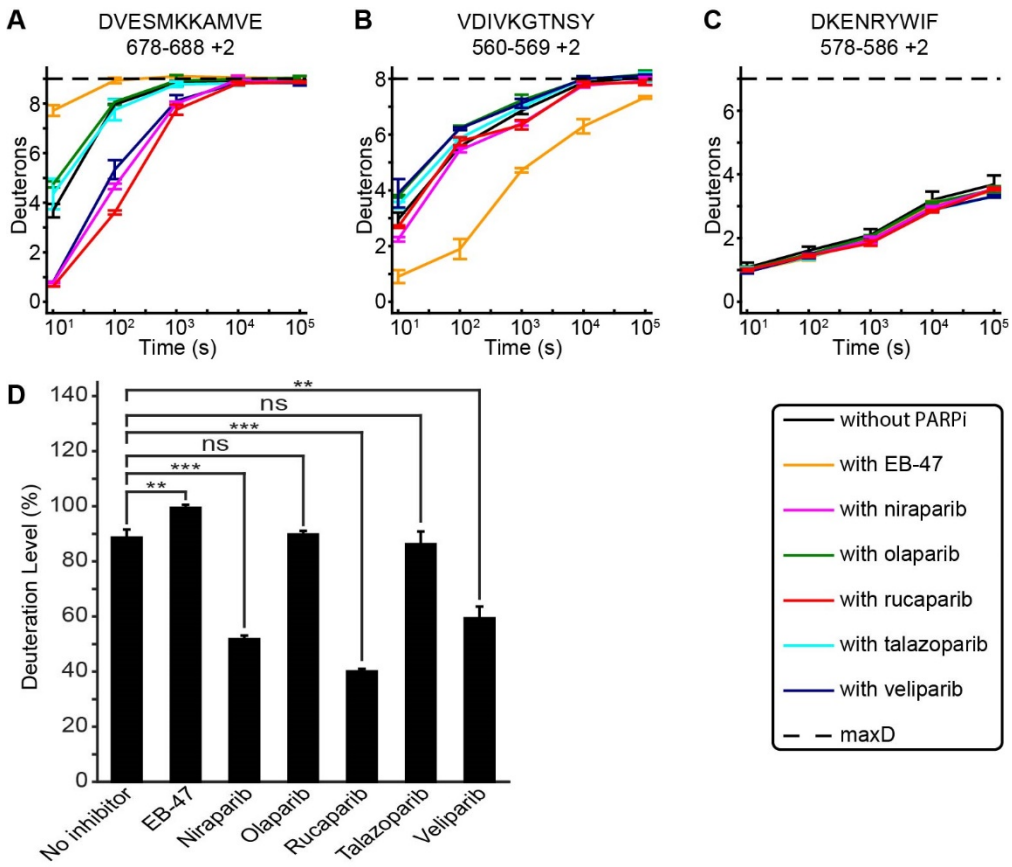

Figure S3: Peptide deuteration curves for the representative peptides from different regions of PARP-1. Deuteration curves for representative peptides from (A) αB helix of HD domain (region iv in Fig. 1B), (B) allosteric contact region between Zn1-WGR-HD (region i in Fig. 1B), and (C) WGR domain (region i in Fig. 1B). Curves are shown for PARP-1/DNA complex alone, or in the presence of one of the inhibitors, for each timepoint. Each point is an average of three measurements. The level of deuteration was adjusted relative to fully deuterated (FD) sample (see methods for details). Error bars represent s.d. from three independent measurements. Panel A illustrates three distinct behaviors for the inhibitors. Even after 10 s of deuteration, the EB-47 sample is already at 85% deuteration level. Samples with olaparib and talazoparib require 100 s to reach the same levels of deuteration, and an even longer 1000 s for samples with veliparib, rucaparib and niraparib. The peptide from the allosteric contact region in panel B shows that the presence of EB-47 slows down the HX rate in that region almost 100-fold. The peptide in panel C is used as an example to demonstrate the similarity of HX rates for the peptides that are not affected by binding of the inhibitors. (D) Level of deuteration after 100 s of exchange for the αB peptide from panel (A) (678-688 +2). Error bars are calculated as standard deviation from three measurements.

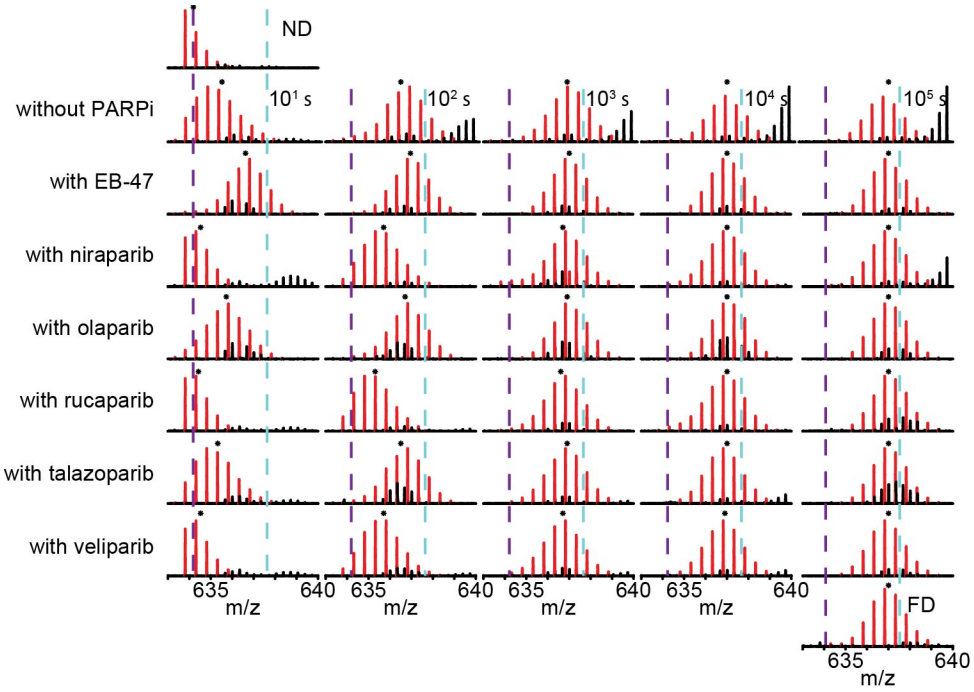

Figure S4: Raw MS spectra for a representative peptide (678 – 688 cs +2) from HD domain. Spectra are shown for the PARP-1/DNA complex alone, or in the presence of each of the designated inhibitors, for each timepoint. Red isotopic envelopes represent the indicated peptides, while black isotopic envelopes are from other co-eluting peptides (note their charge states differ from the peptides of interest) in the same m/z region. Centroid values are indicated using asterisks. Blue and purple dotted lines serve as guides for visualizing differences in relative mass changes at each time point. ND represents the non-deuterated sample. FD represents the "fully-deuterated" sample. Major differences in deuteration can be observed at earlier time points (10-100 s).

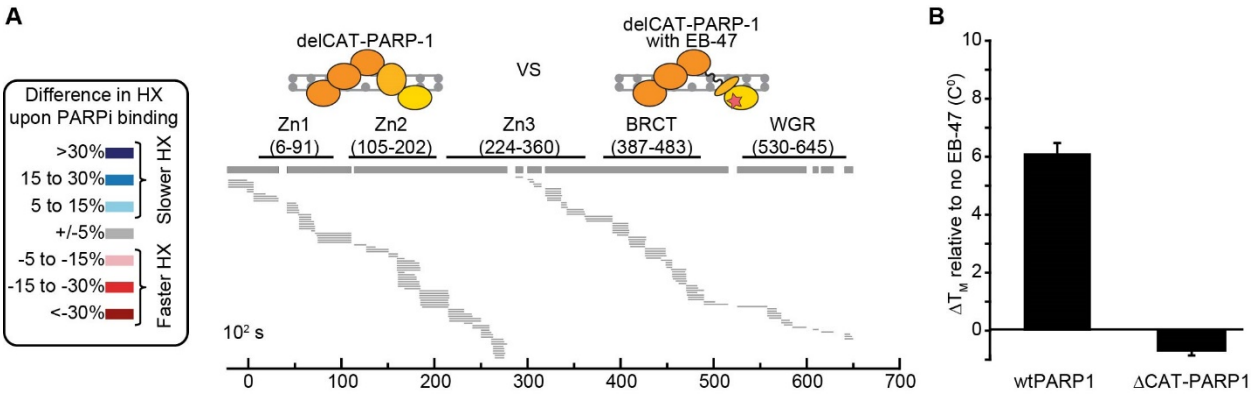

Figure S5: Binding of EB-47 to ΔCAT-PARP-1/SSB-DNA complex. To test whether or not increased protection from HX at the interdomain interaction sites were caused by an allosteric effect, rather than a result of a nonspecific binding, we compared HX rates between PARP-1 mutant ΔCAT (a.a. 1-662) lacking the catalytic domain with and without EB-47 (panel A). Since this mutant lacks the inhibitor binding site, there should be no additional protection of interdomain contacts in the presence of EB-47. Indeed, a plot of percent difference in HX between samples with and without EB-47 show no change in the exchange rates for any of the peptides, indicating that EB-47 does not bind to PARP-1 without CAT domain. Additionally, we compared the DSF thermal stability differences of WT PARP-1 and ΔCAT-PARP-1 with and without EB-47 (panel B). EB-47 substantially increases the melting temperature of wtPARP-1, while for ΔCAT-PARP-1, EB-47 has little effect, supporting the conclusion that there is no interaction between EB-47 and PARP-1 without CAT.

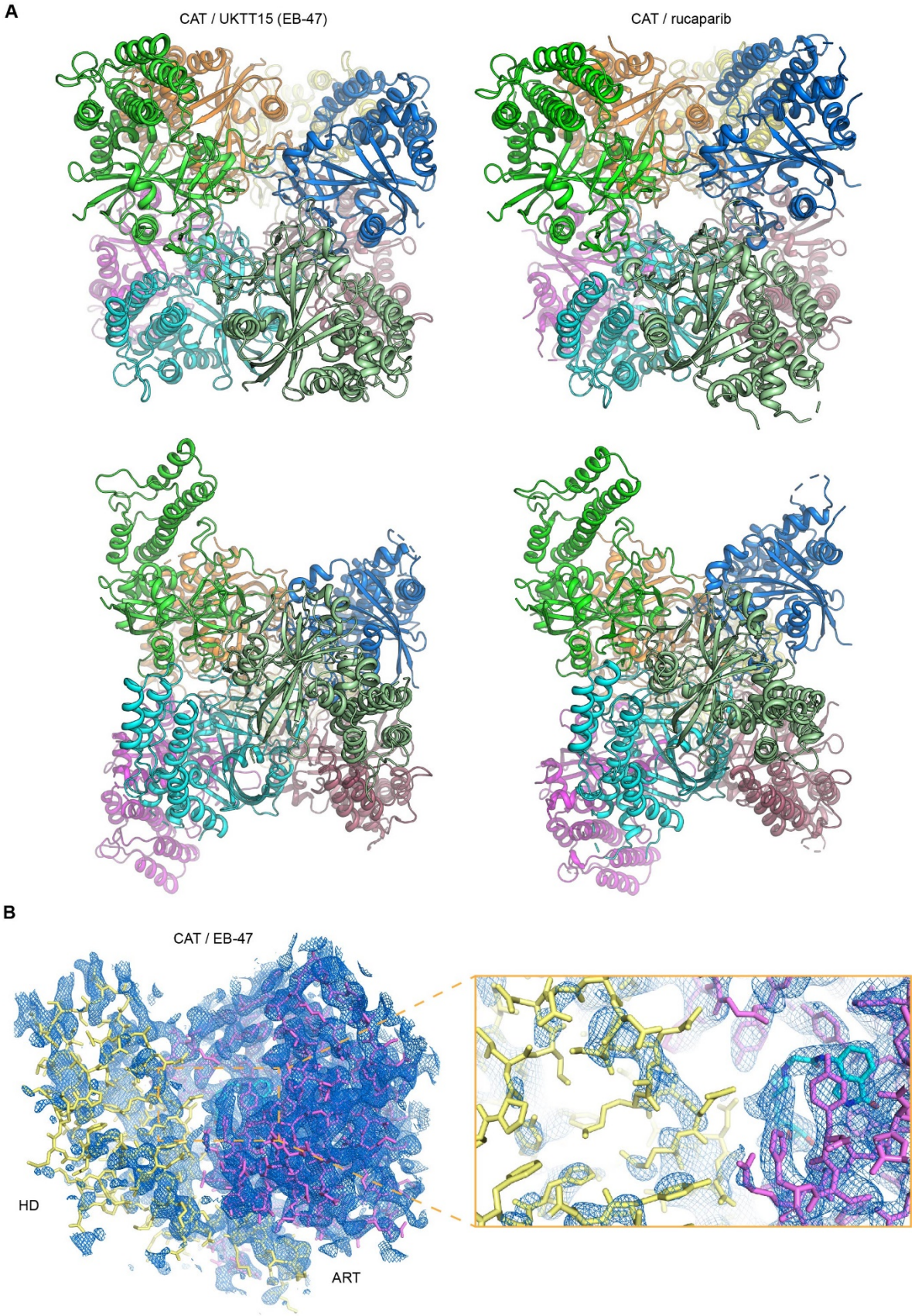
A
CAT / UKTT15 (EB-47)
CAT / rucaparib
B
CAT / EB-47
HD
ART

Figure S6: Crystal structures of PARP-1 CAT with UKTT15 and rucaparib. (A) Two orthogonal views showing that the overall packing arrangement of the CAT/rucaparib structure is similar to that of the CAT/UKTT15 structure (as well as CAT/EB-47), despite the crystals belonging to different space groups (see crystallographic statistics in Table S2). (B) The weighted $2F_O$-F_C electron density map of the CAT/EB-47 complex shows weaker electron density for the HD domain relative to the ART, illustrating how the HD conformation is perturbed/poorly ordered in the presence of EB-47, in contrast to the CAT/rucaparib complex, as seen in Fig. 4H. EB-47, which was designed to mimic NAD^+ (*28*), which does not bind to PARP-1 unless the HD is unfolded or deleted. Moreover, the crystal structure of PARP-2 CAT ΔHD bound to EB-47 predicted clashes between residues of the HD and EB-47 (*4*). Thus, the ability of EB-47 to bind PARP-1 CAT with a folded HD was somewhat surprising (Fig. 1D). However, the ~1000-fold higher affinity of EB-47 relative to BAD could override the HD clashes. The crystal structure of CAT/EB-47 illustrates the perturbations to HD structure and EB-47 conformation that permit binding (see also Fig. S13A,B), and indicate the structural basis for EB-47 influence on PARP-1 allostery. For clinical PARPi, their smaller size compared to NAD^+/BAD is likely to explain why they do not need the HD to be deleted in order to bind to the PARP-1 active site (Fig. 1D).

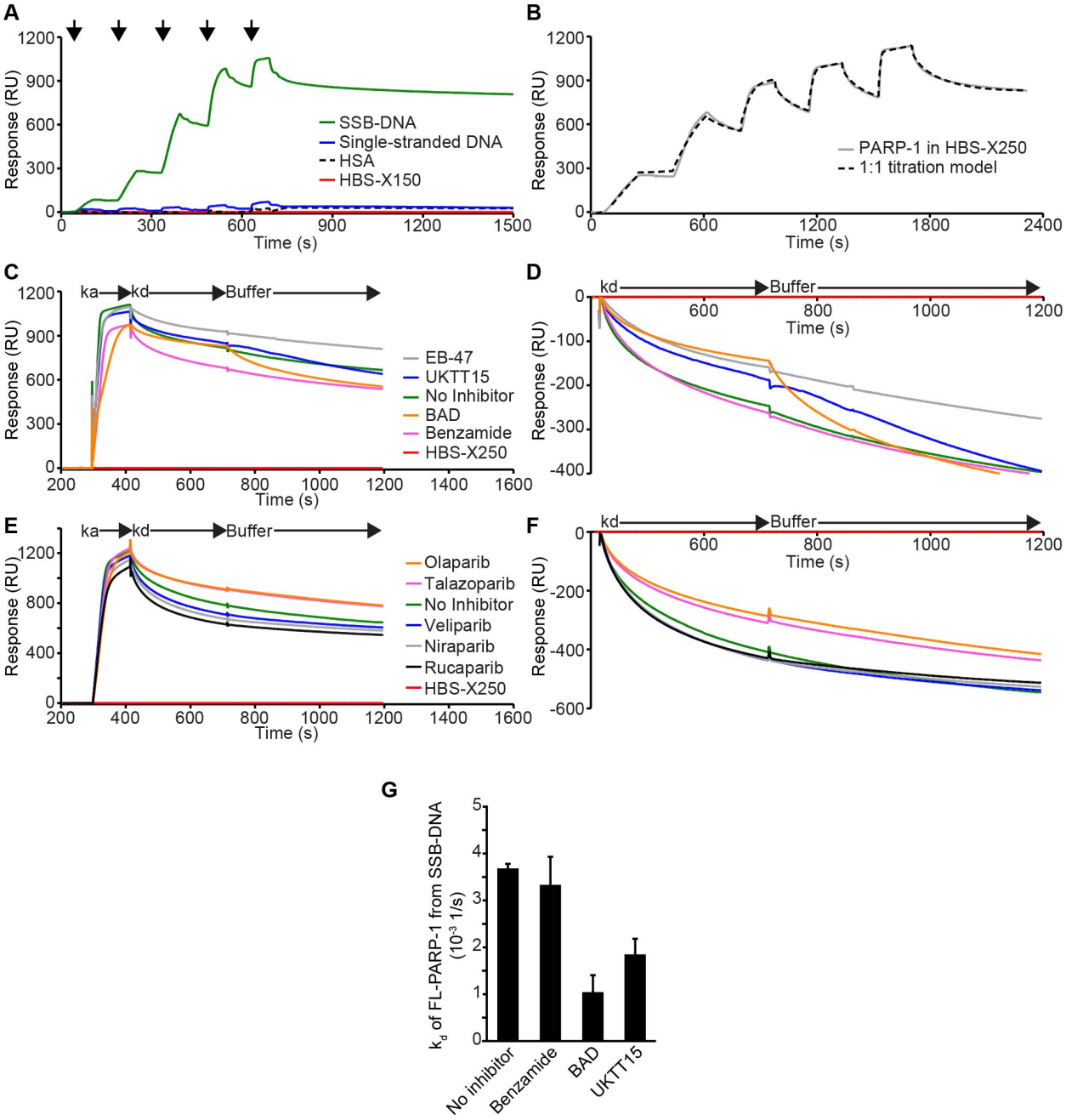

Figure S7: SPR studies to investigate PARP-1 binding to DNA in the presence of inhibitors. (A) Dose-dependent binding of PARP-1 (black arrows: 3.13, 6.25, 12.5, 25, 50 nM) is structure specific for SSB-DNA and not a single strand of DNA in 150 mM NaCl buffer (HBS-X150). Also, as a negative control, there was no binding of HSA to SSB-DNA. (B) Experiments were performed in buffer HBS-X250 to reduce non-specific interactions and to yield the expected 1:1 binding profile. (C, E) Fixed PARP-1 concentration (30 nM) binding to SSB-DNA in the absence (buffer only) or presence of inhibitors (both association (k_a) and dissociation (k_d) phases) followed by additional "wash out" period (buffer only, no inhibitors). (D, F) The data from C and E are re-

aligned to zero around the 400 s mark in panel D and F, respectively, to compare the dissociation kinetics and wash out period. (G) Apparent dissociation rate constant k_d of PARP-1 from SSB-DNA measured by SPR in the presence of BAD, benzamide or UKTT15. Dissociation rate constants for the clinical inhibitors are shown in Fig. 1F. Note that the SPR experiments are monitoring PARP-1 dissociation from DNA, whereas the FP competition experiments (e.g. Fig. 3C) are monitoring PARP-1 exchange from labeled DNA to unlabeled DNA, thus giving rise to differences in apparent dissociation kinetics that are due to the different experimental setups.

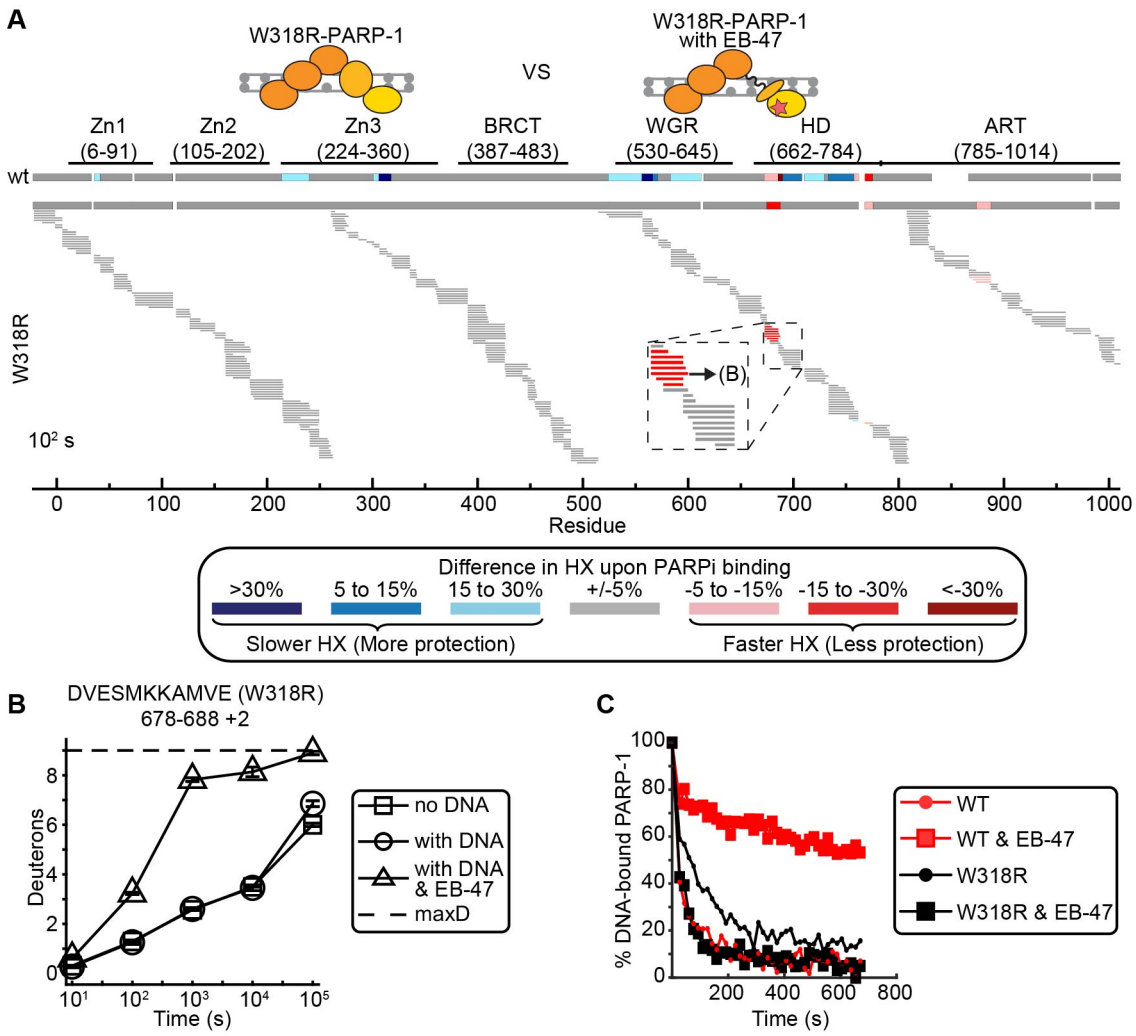

Figure S8: W318R mutation disrupts reverse allostery. (A) Percent difference in HX upon binding EB-47 was calculated for each peptide in W318R mutant version of PARP-1 and displayed in a similar manner as in Fig. 3A. A plot of the consensus HX differences for WT PARP-1 is shown on the top, and the consensus plot is also shown for W318R. (B) HX of a specific peptide from the αB helix of the HD for W318R mutant PARP-1 (same peptide as in Fig. 3B). Error bars represent s.d. from three measurements. (C) FP DNA competition experiments with WT and W318R versions of PARP-1 bound to SSB-DNA with or without EB-47. In our FP competition assays, PARP-1 is bound to a fluorescently labelled DNA probe. An unlabeled, identical DNA fragment is then added and PARP-1 release from the probe is measured over time as a decrease in FP. We have previously shown that BAD can increase retention of PARP-1 on DNA in this type of experiment (*6*).

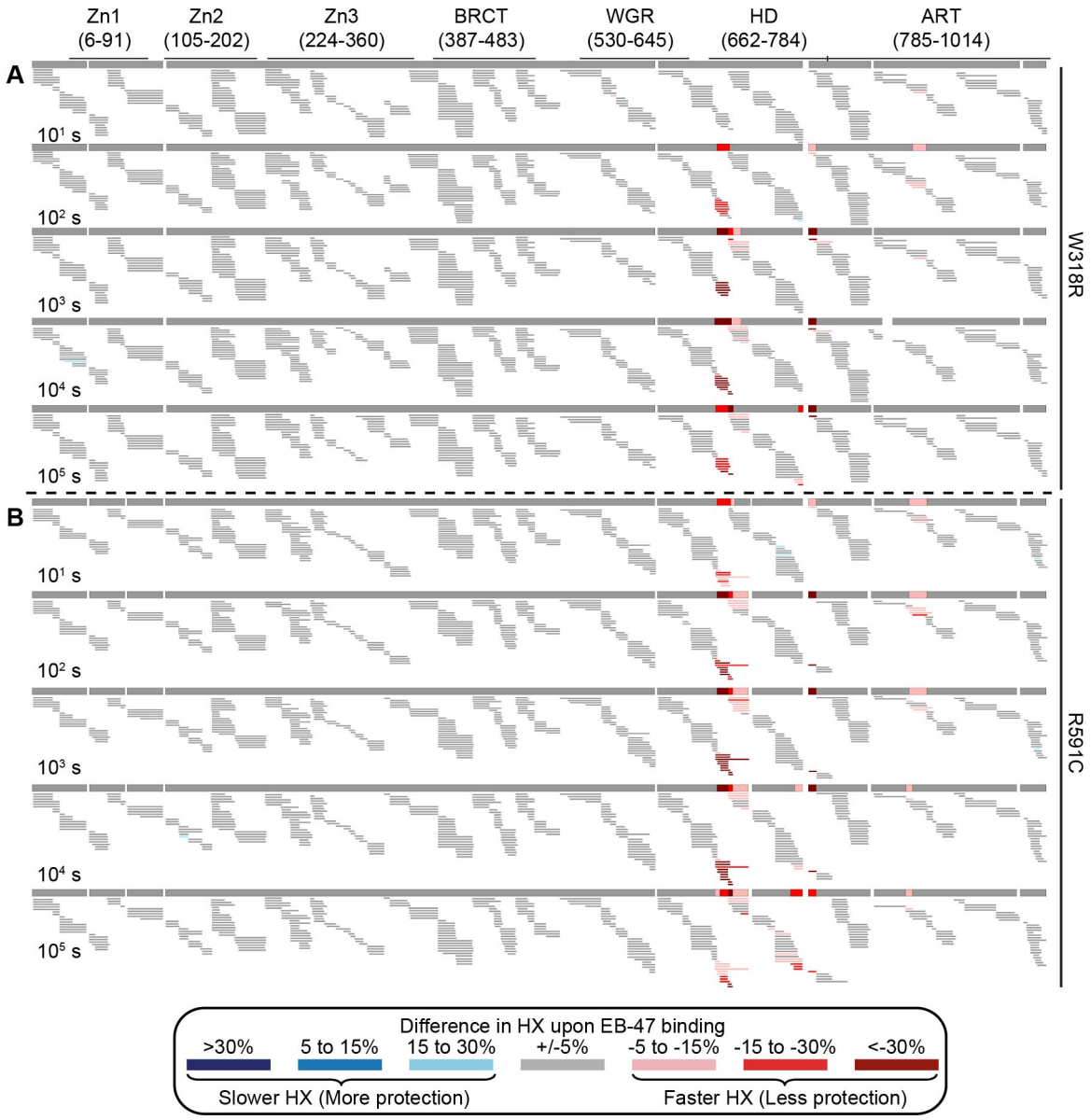

Figure S9: Difference plots representing the changes in HX rates for W318R (A) and R591C (B) complexes with PARP-1/SSB-DNA in the presence versus absence of EB-47. The coloring indicates the changes in HX rates in peptides upon EB-47 binding. This figure shows data for all five time points collected. Data for the 100 s time point are also shown in Figs. 3A and S8.

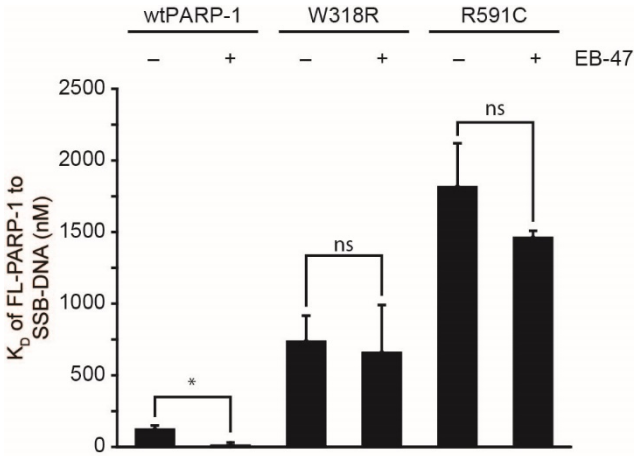

Figure S10: SSB-DNA binding affinities of PARP-1 mutants in the presence of EB-47. HXMS data, as well as the competition assay in Fig. 3, indicate that disruption of the allosteric communication via W318R and R591C mutations prevents EB-47 from slowing down the release of PARP-1 from SSB-DNA or from increasing protection at inderdomain interfaces. To test whether or not the increased binding affinity of PARP-1 to SSB-DNA in the presence of EB-47 observed in Fig. 1F was also a result of reverse-allostery, we measured apparent equilibrium binding affinity K_D of (A) WT PARP-1, (B) W318R, or (C) R591C to SSB-DNA by FP in the absence or presence of EB-47. The presence of EB-47 reduced the K_D of the WT PARP-1, but the binding of W318R and R591C are unaffected, indicating that indeed stronger PARP-1 binding to SSB-DNA is done through reverse-allosteric communication. Error bars represent s.d. from three independent experiments.

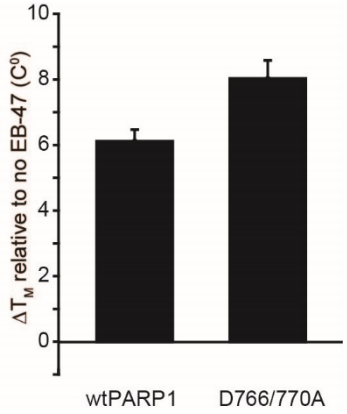

Figure S11: Thermal stability of D766/770A-PARP-1 with or without EB-47. The DSF melting temperature of D766/770A-PARP-1 is increased (ΔT_M) by EB-47 binding to a similar extent as is WT PARP-1. Error bars represent s.d. from three independent experiments.

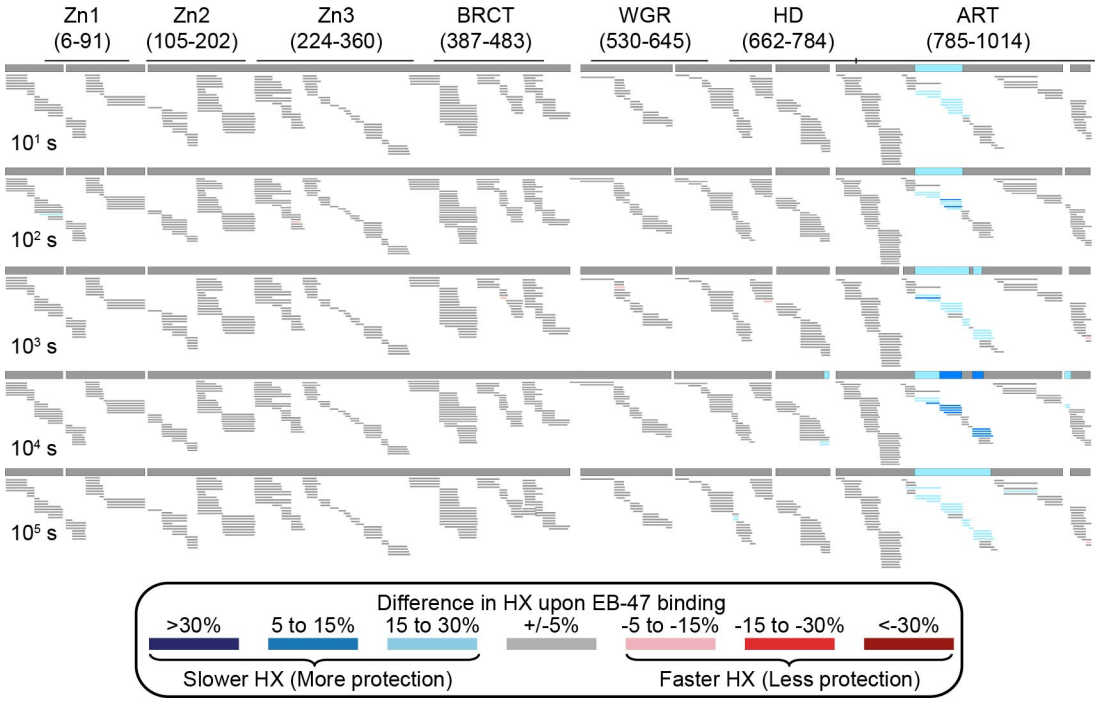

Figure S12: Difference plots representing the changes in HX rates for D766/770A PARP-1/SSB-DNA complexes upon binding EB-47. The coloring indicates the changes in HX rates in peptides upon EB-47 binding. This figure shows data for all five time points collected. Data for the 100 s time point is also shown in Fig. 3A.

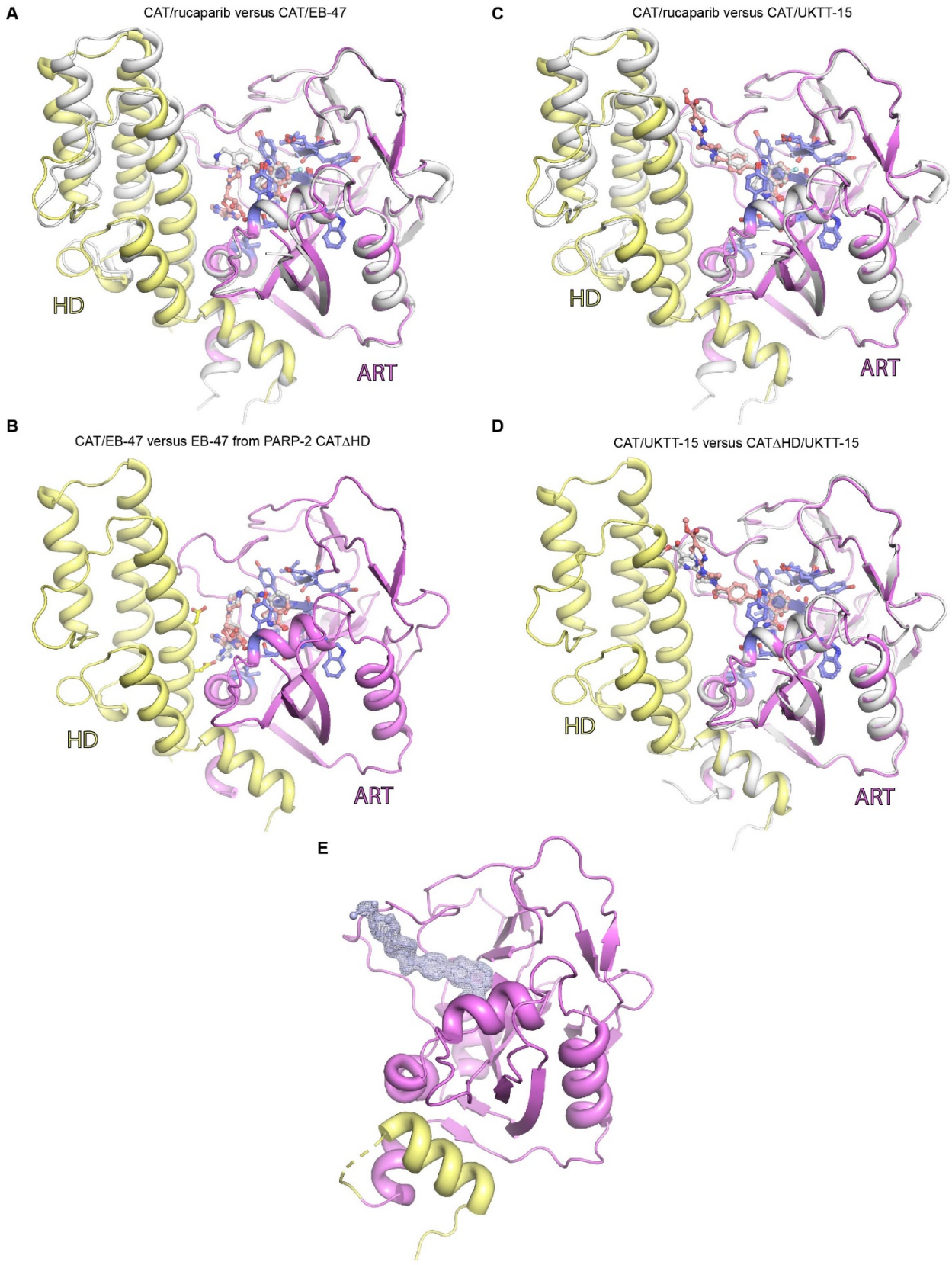
A
CAT/rucaparib versus CAT/EB-47
HD
ART
C
CAT/rucaparib versus CAT/UKTT-15
HD
ART
B
CAT/EB-47 versus EB-47 from PARP-2 CATΔHD
HD
ART
D
CAT/UKTT-15 versus CATΔHD/UKTT-15
HD
ART
E

Figure S13: Comparisons of CAT structures with different inhibitors. (A) Alignment of PARP-1 CAT/rucaparib (both PARP-1 and rucaparib in white) to PARP-1 CAT/EB-47 (PARP-1 yellow/magenta, EB-47 light pink) shows how the HD is displaced away from the ART in the presence of EB-47 compared to rucaparib. In each panel, structures were aligned using the ART residues drawn as blue sticks. (B) View of the PARP-1 CAT/EB-47 structure (yellow/magenta/light pink, as above), overlayed with the EB-47 molecule (in white) derived from the PARP2 CATΔHD/EB-47 structure. The comparison of EB-47 conformations illustrates how the adenine moiety of EB-47 pivots due to clashes with the HD in the CAT/EB-47 structure. HD residues D766 and D770 are drawn as sticks and colored yellow. (C) Alignment of the CAT/rucaparib structure (colored as in panel A) to the CAT/UKTT-15 structure (PARP-1 yellow/magenta, UKTT-15 light pink) shows how the HD is displaced away from the ART in the presence of UKTT-15 compared to rucaparib. The ART loop adjacent to the HD is also re-positioned near the UKTT-15 extension toward the HD. (D) Alignment of CAT/UKTT-15 (color as in panel C) and CATΔHD/UKTT-15 (both PARP-1 and UKTT-15 in white) indicates similar overall binding conformations for UKTT-15 in both structures, but highlights how the UKTT-15 extension is repositioned to accommodate the presence of the HD. (E) Crystal structure of the PARP-1ΔHD in complex with UKTT15. A weighted F_O-F_C difference electron density map (bluewhite) is shown contoured at 3σ around UKTT15 (bluewhite), illustrating the density present prior to the modeling of UKTT15. This panel is an expanded version of Fig. 4F.

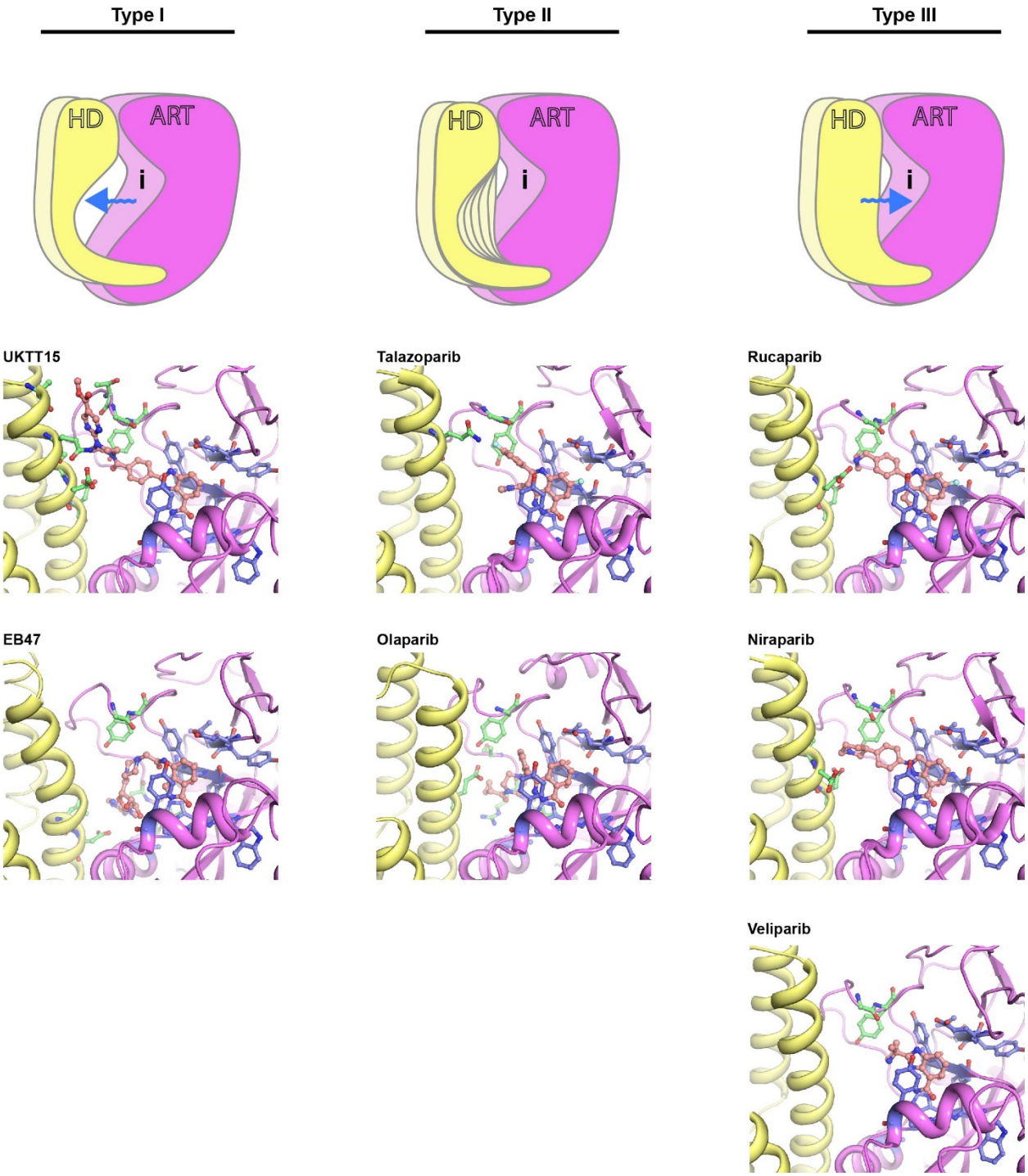

Figure S14: PARPi interaction with the HD. We aligned PARP-1/PARPi structures based on their allosteric classification to illustrate the expected impact on the HD. In all images, ART residues that form the binding site are drawn in blue sticks, and HD residues that that have atoms within 4 Å of the bound PARPi are drawn as green sticks. The binding positions of Type I compounds, such as EB-47 and UKTT-15, are in conflict with the HD (represented by a blue arrow pointing toward the HD in the cartoon image). In our crystal structures of these complexes, the HD appears to be poorly ordered/highly mobile (Figure 4H and S6). When PARP-1 is bound to DNA, these conflicts with the HD

promote the HD unfolded state and thereby promote DNA binding by the regulatory domains. The binding positions of Type II compounds, such as talazoparib and olaparib, are not in conflict with the HD and therefore have little to no effect on PARP-1 allostery and DNA binding ability. The cartoon shows a mobile HD that is largely not influenced by the Type II compound. Our results and the structures suggest that further extensions to these molecules could convert them to Type I molecules. The binding positions of Type III compounds, such as niraparib and rucaparib, contact the HD but we infer that these are “positive” contacts that support the folded conformation of the HD (represented by blue arrow to the right in the cartoon), and therefore decrease the ability of PARP-1 to bind DNA. In contrast, veliparib does not directly contact the HD. We surmise that the binding pose of veliparib stabilizes the ART fold in a way that supports ART interaction with the HD. While the crystal structures provide valuable information on contacts between PARP-1 and the various inhibitors, the structures provide static views that do not capture the dynamics of PARP-1, highlighting the importance of our biophysical and biochemical analysis that directly probes the effects of these inhibitors.

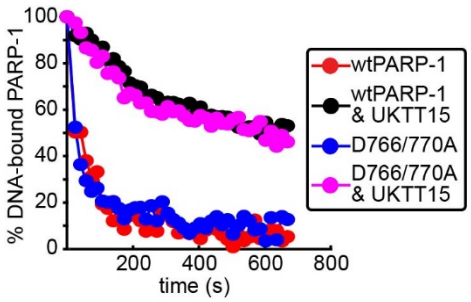

Figure S15: Fluorescence polarization DNA competition experiments. The DNA release kinetics were examined for WT or D766/770A PARP-1 in complex with SSB-DNA in the presence or absence of UKTT15.

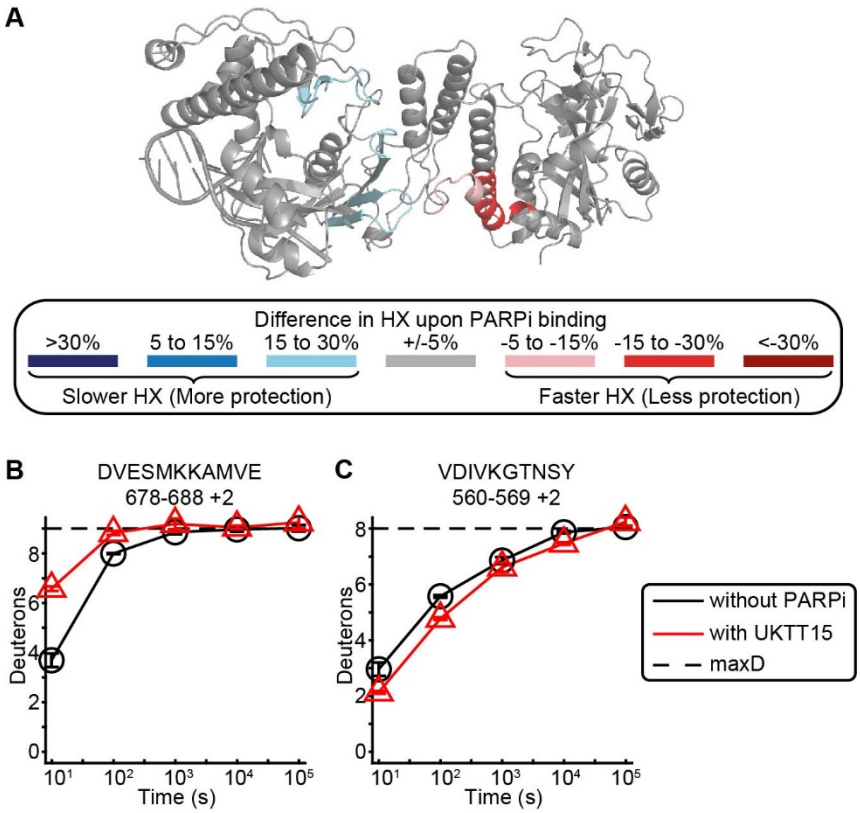

Figure S16: HXMS data for PARP-1/SSB-DNA complex in presence of UKTT15. (A) Consensus difference HXMS data upon binding of UKTT15 at 100 s shown in Fig. 4E mapped on PARP-1 structure. (B), (C) representative peptides from (B) αB helix of HD domain (region iv in Fig. 1B) and (C) allosteric contact region between Zn1-WGR-HD (region i in Fig. 1B). Peptide in panel B shows increased deuteration in the presence of UKTT15, indicating unfolding of HD. On the other hand, peptide in panel C shows reduced deuteration, indicating increased protection at the inter-domain interaction interface.

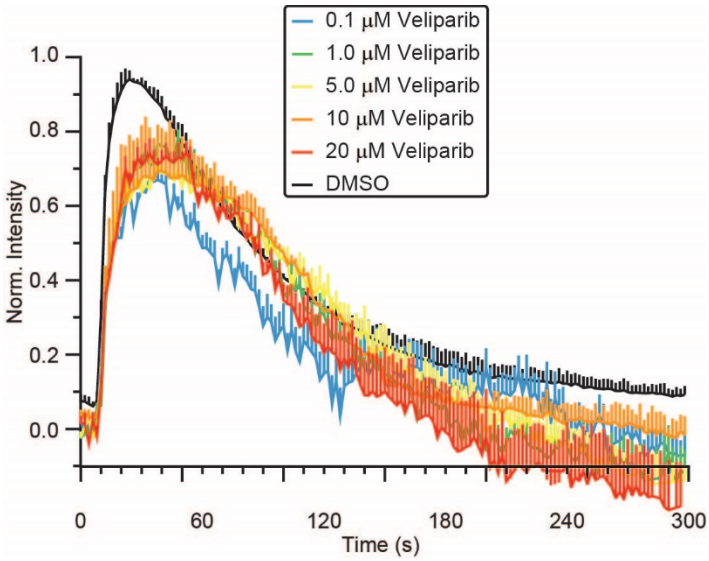

Figure S17: Dose dependence of kinetics of PARP-1 trapping at sites of DNA damage in cells in presence of veliparib. This experiment was performed as in Fig. 5C,D, but in the presence of 0.1-20 μM veliparib. We assessed the trapping ability of PARPi in cells using an established laser microirradiation assay (*46*, *55*). PARP-1$^{-/-}$ CAL51 cells were reconstituted with PARP-1-GFP expressing cDNA constructs and subjected to localized irradiation with a UV laser, which causes localized generation of DNA damage and recruitment of PARP-1.

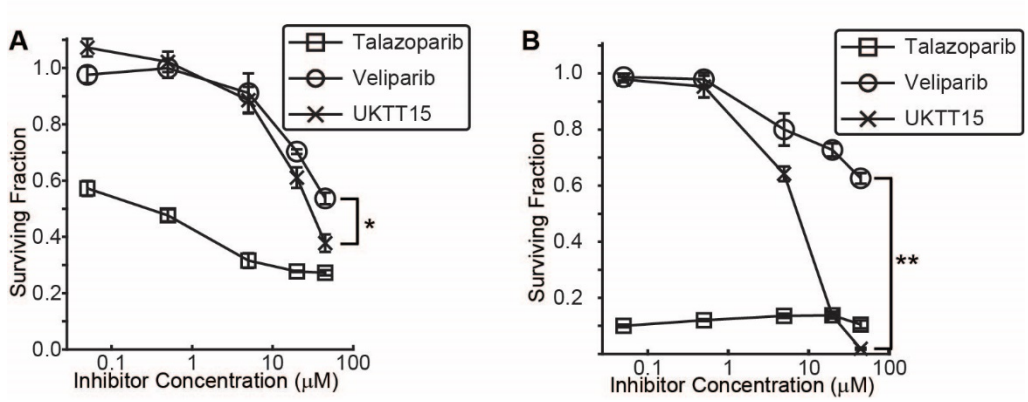

Figure S18: Survival assays for SUM149PT and CAPAN-1 cells. (A), (B) Survival assay for CAPAN-1 (A) and SUM149PT (B) cells in the presence of an increasing concentration of veliparib, talazoparib or UKTT15, as indicated.

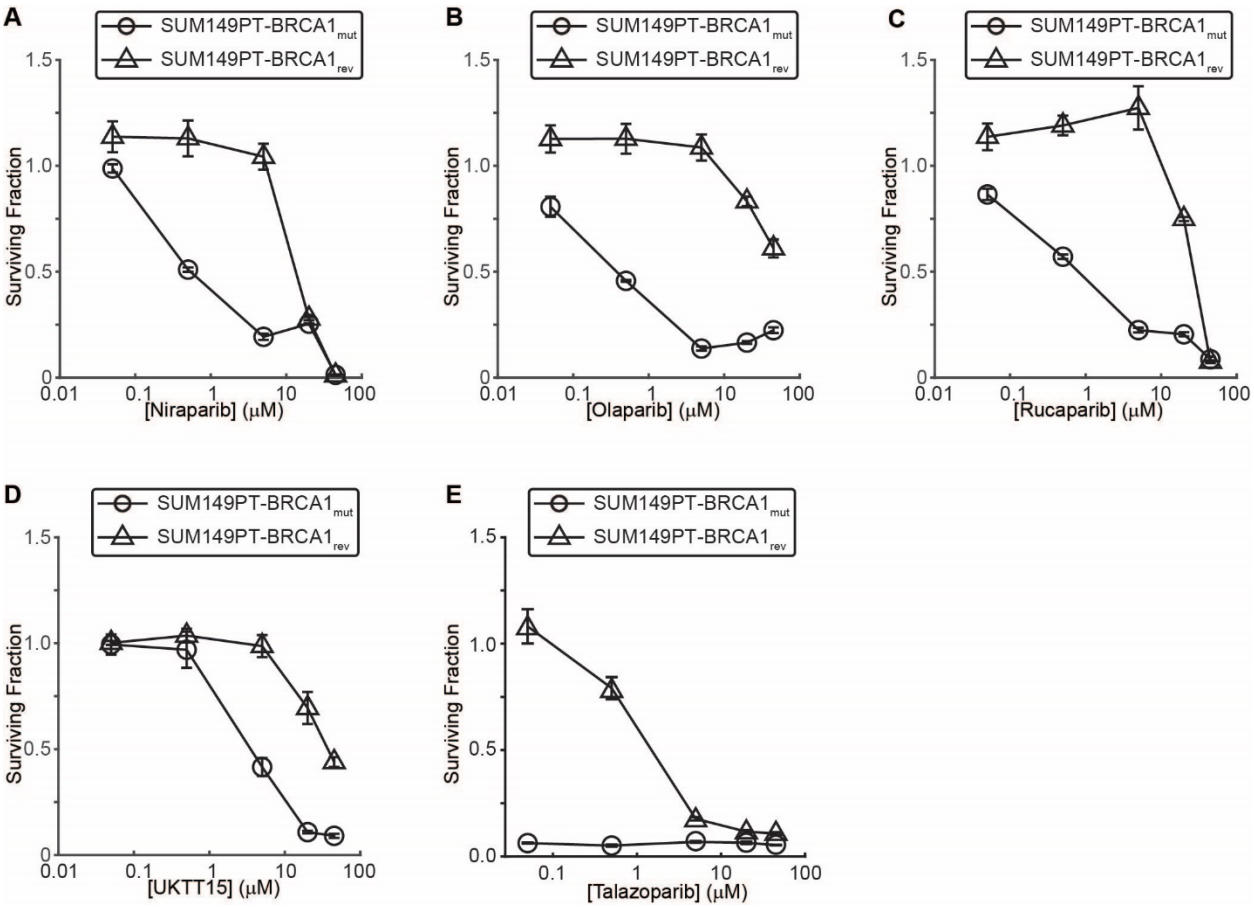

Figure S19: Survival assay for SUM149PT-BRCA1^{mut} and SUM149PTBRCA1^{rev} cells. The experiments were performed as in Fig. 5E, in the presence of (A) niraparib, (B) olaparib, (C) rucaparib, (D) UKTT15, or (E) talazoparib.

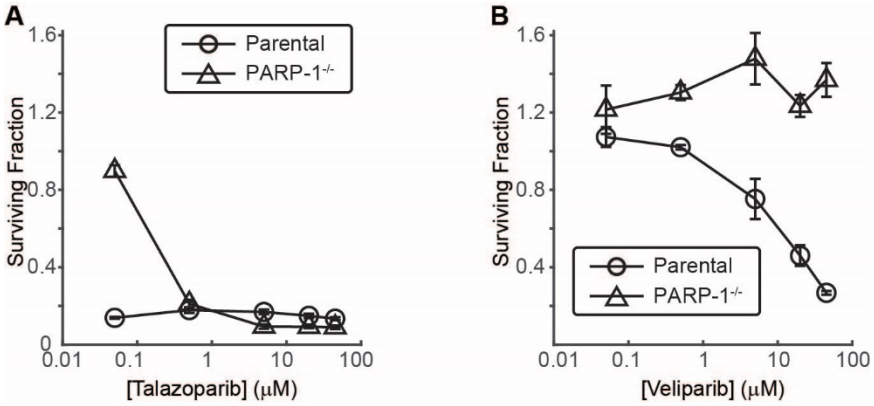

Figure S20: Survival assays for the parental or PARP-1$^{-/-}$ cells. The experiments were performed as in Fig. 5F, in the presence of (A) talazoparib or (B) veliparib.

Table S1. Comparison of individual dissociation rate constants (kd) for PARP-1 binding to SSB-DNA in the absence or presence of inhibitors. Replicate measurements (n) were averaged and standard deviations (SD) are indicated, and also reported in Fig. 1F. The PARP-1 only injection at the start of each titration series (normalized to 1.00) was in good agreement with the PARP-1 injection performed at the end of each titration series (1.01-fold change in calculated k_d). PARPi had differential effects on the dissociation rates, for example, EB-47 decreased the dissociation rate by approximately 65% (0.35-fold change) whereas rucaparib increased it by approximately 40% (1.42-fold change).

Co-injection	k_d (s^{-1})	+/- SD	fold change	n
+ EB-47	1.14E-03	4.92E-04	0.35	9
+ BAD	1.35E-03	3.66E-04	0.40	11
+ UKTT15	1.85E-03	3.48E-04	0.55	6
+ Olaparib	2.31E-03	1.00E-05	0.69	3
+ Talazoparib	2.52E-03	1.53E-05	0.75	3
+ Benzamide	3.28E-03	6.14E-04	0.98	8
PARP-1 start	3.36E-03	8.06E-05	**1.00**	14
PARP-1 end	3.39E-03	2.66E-04	1.01	14
+ Veliparib	4.08E-03	6.24E-05	1.21	3
+ Niraparib	4.40E-03	3.46E-05	1.31	3
+ Rucaparib	4.77E-03	4.51E-05	1.42	3

Table S2. Crystallographic data and refinement statistics

Data Collection[a]				
PARP-1 structure	**CATΔHD / UKTT15**	**CAT / UKTT15**	**CAT / EB47**	**CAT / Rucaparib**
Space Group	$P6_122$	C2	C2	$P2_12_12_1$
PDB code	6NTU	6VKO	6VKQ	6VKK
Unit Cell Dimensions	*a*=*b*=92.7,*c*=135.3 Å α=β=90,γ=120°	*a*=140,*b*=130,*c*=103 Å α=γ=90,β=111°	*a*=140,*b*=130,*c*=102 Å α=γ=90,β=111°	*a*=104,*b*=108,*c*=143 Å α=γ=β=90°
	1 molecule / asu	4 molecules / asu	4 molecules / asu	4 molecules / asu
Wavelength (Å)	0.979	0.979	0.979	0.979
Resolution range (Å)	50.0–1.7 (1.73–1.7)	50.0–2.8 (2.95–2.8)	50.0–2.9 (3.06–2.9)	50.0–2.1 (2.14–2.1)
Completeness (%)	100.0 (100.0)	95.4 (95.5)	99.7 (99.7)	99.8 (100.0)
Unique observations	33,747 (1,760)	39,994 (5,800)	37,721 (5,472)	94,458 (4,678)
Average Redundancy	27.9 (27.4)	4.6 (4.5)	5.6 (5.5)	11.7 (12.3)
Mean (I/σI)[b]	24.7 (1.9)	5.3 (1.8)	8.3 (2.1)	16.3 (2.0)
R_{merge} (%)[b]	6.9 (160.0)	15.2 (70.9)	12.5 (65.0)	8.3 (128.8)
R_{pim} (%)[b]	1.3 (30.8)	7.6 (35.9)	2.9 (42.0)	2.8 (55.5)
Mean I CC(1/2)[b]	1.0 (0.841)	0.974 (0.747)	0.996 (0.887)	0.998 (0.778)
Model Refinement[a]				
Resolution Range (Å)	50.0–1.7 (1.74–1.7)	20.0–2.8 (2.87–2.8)	20.0–2.9 (2.97–2.9)	20.0–2.1 (2.15–2.1)
Number of reflections	32,018 (2,336)	37,777 (2,709)	35,580 (2,573)	89,014 (6,550)
R [c]	0.159 (0.262)	0.284 (0.325)	0.323 (0.388)	0.239 (0.293)
R_{free}[c]	0.182 (0.250)	0.312 (0.330)	0.353 (0.387)	0.261 (0.310)
Number of atoms / Average B-factor (Å^2)	2,147 / 40.0	10,970 / 98.2	10,910 / 85.1	11,126 / 59.4
protein	1,937 / 39.2	10,735 / 98.5	10,694 / 85.4	10,798 / 59.7
solvent	184 / 48.1	91 / 78.4	60 / 70.0	232 / 59.2
inhibitor	26 / 40.8	144 / 89.0	156 / 70.6	96 / 39.6
Phi/Psi, favored (%) / outliers (%)[d]	97.8 / 0	91.2 / 0.89	98.3 / 0	85.6 / 3.4
Rmsd bond angles (°)	1.31	1.47	1.40	1.24
Rmsd bond lengths (Å)	0.009	0.006	0.004	0.004

[a] Values in parentheses refer to data in the highest resolution shell.

[b] As calculated in SCALA[37] : $R_{merge} = \sum_{hkl}\sum_j |I_j - \langle I\rangle| \; / \; \sum_{hkl}\sum_j I_j$. $\langle I\rangle$ is the mean intensity of *j* observations of reflection *hkl* and its symmetry equivalents; R_{pim} takes into account measurement redundancy when calculating R_{merge}; Mean I CC(1/2) is the correlation between mean intensities calculated for two randomly chosen half-sets of the data.

[c] $R = \sum_{hkl} |F_{obs} - kF_{calc}| / \sum_{hkl} |F_{obs}|$ for reflections used in refinement. R_{free} = R for 5% of reflections excluded from crystallographic refinement.

[d] As reported in PHENIX.

References

40. T. D. Penning, G.-D. Zhu, V. B. Gandhi, J. Gong, X. Liu, Y. Shi, V. Klinghofer, E. F. Johnson, C. K. Donawho, D. J. Frost, V. Bontcheva-Diaz, J. J. Bouska, D. J. Osterling, A. M. Olson, K. C. Marsh, Y. Luo, V. L. Giranda, Discovery of the Poly(ADP-ribose) polymerase (PARP) inhibitor 2-[(R)-2-methylpyrrolidin-2-yl]-1H-benzimidazole-4-carboxamide (ABT-888) for the treatment of cancer. *J. Med. Chem.* **52**, 514–523 (2009).

41. T. A. Hopkins, W. B. Ainsworth, P. A. Ellis, C. K. Donawho, E. L. DiGiammarino, S. C. Panchal, V. C. Abraham, M. A. Algire, Y. Shi, A. M. Olson, E. F. Johnson, J. L. Wilsbacher, D. Maag, PARP1 Trapping by PARP Inhibitors Drives Cytotoxicity in Both Cancer Cells and Healthy Bone Marrow. *Mol. Cancer Res. MCR* (2018), doi:10.1158/1541-7786.MCR-18-0138.

42. L. Liu, M. Kong, N. R. Gassman, B. D. Freudenthal, R. Prasad, S. Zhen, S. C. Watkins, S. H. Wilson, B. Van Houten, PARP1 changes from three-dimensional DNA damage searching to one-dimensional diffusion after auto-PARylation or in the presence of APE1. *Nucleic Acids Res.* **45**, 12834–12847 (2017).

43. M.-F. Langelier, A. A. Riccio, J. M. Pascal, PARP-2 and PARP-3 are selectively activated by 5’ phosphorylated DNA breaks through an allosteric regulatory mechanism shared with PARP-1. *Nucleic Acids Res.* **42**, 7762–7775 (2014).

44. D. G. Myszka, Improving biosensor analysis. *J. Mol. Recognit. JMR*. **12**, 279–284 (1999).

45. R. Karlsson, P. S. Katsamba, H. Nordin, E. Pol, D. G. Myszka, Analyzing a kinetic titration series using affinity biosensors. *Anal. Biochem.* **349**, 136–147 (2006).

46. O. Mortusewicz, L. Schermelleh, J. Walter, M. C. Cardoso, H. Leonhardt, Recruitment of DNA methyltransferase I to DNA repair sites. *Proc. Natl. Acad. Sci. U. S. A.* **102**, 8905–8909 (2005).

47. W. Kabsch, XDS. *Acta Crystallogr. D Biol. Crystallogr.* **66**, 125–132 (2010).

48. A. J. McCoy, R. W. Grosse-Kunstleve, P. D. Adams, M. D. Winn, L. C. Storoni, R. J. Read, Phaser crystallographic software. *J. Appl. Crystallogr.* **40**, 658–674 (2007).

49. P. D. Adams, P. V. Afonine, G. Bunkóczi, V. B. Chen, I. W. Davis, N. Echols, J. J. Headd, L.-W. Hung, G. J. Kapral, R. W. Grosse-Kunstleve, A. J. McCoy, N. W. Moriarty, R. Oeffner, R. J. Read, D. C. Richardson, J. S. Richardson, T. C. Terwilliger, P. H. Zwart, PHENIX: a comprehensive Python-based system for macromolecular structure solution. *Acta Crystallogr. D Biol. Crystallogr.* **66**, 213–221 (2010).

50. M. D. Winn, C. C. Ballard, K. D. Cowtan, E. J. Dodson, P. Emsley, P. R. Evans, R. M. Keegan, E. B. Krissinel, A. G. W. Leslie, A. McCoy, S. J. McNicholas, G. N.

Murshudov, N. S. Pannu, E. A. Potterton, H. R. Powell, R. J. Read, A. Vagin, K. S. Wilson, Overview of the CCP4 suite and current developments. *Acta Crystallogr. D Biol. Crystallogr.* **67**, 235–242 (2011).

51. P. Emsley, B. Lohkamp, W. G. Scott, K. Cowtan, Features and development of Coot. *Acta Crystallogr. D Biol. Crystallogr.* **66**, 486–501 (2010).

52. G. N. Murshudov, P. Skubák, A. A. Lebedev, N. S. Pannu, R. A. Steiner, R. A. Nicholls, M. D. Winn, F. Long, A. A. Vagin, REFMAC5 for the refinement of macromolecular crystal structures. *Acta Crystallogr. D Biol. Crystallogr.* **67**, 355–367 (2011).

53. M.-F. Langelier, J. M. Pascal, PARP-1 mechanism for coupling DNA damage detection to poly(ADP-ribose) synthesis. *Curr. Opin. Struct. Biol.* **23**, 134–143 (2013).

54. M.-F. Langelier, J. L. Planck, S. Roy, J. M. Pascal, Crystal structures of poly(ADP-ribose) polymerase-1 (PARP-1) zinc fingers bound to DNA: structural and functional insights into DNA-dependent PARP-1 activity. *J. Biol. Chem.* **286**, 10690–10701 (2011).

55. D. B. Krastev, S. J. Pettitt, J. Campbell, F. Song, B. E. Tanos, S. S. Stoynov, A. Ashworth, C. J. Lord, Coupling bimolecular PARylation biosensors with genetic screens to identify PARylation targets. *Nat. Commun.* **9**, 2016 (2018).